



**HAL**  
open science

## Reference-free combined XRR-GIXRF analysis at the French Synchrotron SOLEIL

Yves Menesguen, Marie-Christine Lepy

► **To cite this version:**

Yves Menesguen, Marie-Christine Lepy. Reference-free combined XRR-GIXRF analysis at the French Synchrotron SOLEIL. *Physica Status Solidi A*, 2021, pp.2100423. 10.1002/pssa.202100423 . cea-03324651

**HAL Id: cea-03324651**

**<https://cea.hal.science/cea-03324651>**

Submitted on 23 Aug 2021

**HAL** is a multi-disciplinary open access archive for the deposit and dissemination of scientific research documents, whether they are published or not. The documents may come from teaching and research institutions in France or abroad, or from public or private research centers.

L'archive ouverte pluridisciplinaire **HAL**, est destinée au dépôt et à la diffusion de documents scientifiques de niveau recherche, publiés ou non, émanant des établissements d'enseignement et de recherche français ou étrangers, des laboratoires publics ou privés.

# Reference-free combined XRR-GIXRF analysis at the SOLEIL synchrotron

Y. Ménesguen<sup>1</sup> and M.-C. Lépy<sup>1</sup>

<sup>1</sup>Université Paris-Saclay, CEA, LIST, Laboratoire National Henri Becquerel (LNE-LNHB), F-91120 Palaiseau, France

**X-ray reflectometry, spectrometry, grazing incidence x-ray fluorescence, thin films structure**

## Abstract

CASTOR is a new instrument, operated at the SOLEIL synchrotron facility, dedicated to the characterization of thin films with thicknesses in the nanometer range. The instrument can combine x-ray reflectivity (XRR) measurements with fluorescence (XRF) acquisitions and especially total reflection x-ray fluorescence (TXRF) related techniques such as grazing incidence XRF (GIXRF). The instrument is now routinely installed on the hard x-ray branch of the Metrology beamline. Geometrical characterization is presented, reproducibility of measurements is studied and the reference-free GIXRF analysis is described. Some representative examples are given to illustrate the capabilities of the setup and of the combined analysis procedure.

## 1 Introduction

Multilayered thin film stacks with layer thicknesses in the nanometer range have been commonly characterized by x-ray reflectometry (XRR) on synchrotron facilities or with in-lab sources for many years [1]. Reflectivity curves are acquired by varying the incident angle in the grazing incidence regime while recording the intensity of the specular reflected beam. Grazing incidence x-ray fluorescence (GIXRF) is a total reflection x-ray fluorescence analysis (TXRF) related technique [2], which uses the x-ray fluorescence (XRF) angle-dependent intensity at shallow incidence angles. The renewed interest for these techniques came from the elaboration of nanomaterials for applications in power electronics, electricity storage and microelectronics, which require new means of accurate characterization at the nanometer scale. The XRF signal is element-specific and contains information about the elemental composition, concentration profiles and thicknesses. The combination of XRR, sensitive to the electronic density, and GIXRF, sensitive to element density, produces results of better accuracy compared to one technique alone. Some experimental facilities have already been developed to allow GIXRF-XRR combined analysis, using either synchrotron radiation [3, 4] or laboratory x-ray sources [5, 6].

The Laboratoire National Henri Becquerel (LNHB) developed a specific instrument to perform such characterizations at the Metrology beamline of the SOLEIL synchrotron source to propose metrological studies of thin film deposits and support the efforts of institutes or companies in the fast-developing field of nanolayered structures. The instrument CASTOR (Chambre d'Analyse Spectrométrique en Transmission ou en Réflexion - Analysis Chamber for Transmission or Reflection Spectrometry) is a seven axis goniometer based on the model developed at the Physikalisch Technische Bundesanstalt (PTB) and the Technical University of Berlin [3, 7].

This work describes the main parts of the instrument and additional equipment, the experimental conditions at the Metrology beamline of the SOLEIL synchrotron facility and the first results obtained on selected samples.

## 2 Characteristics of the experimental setup

### 2.1 The hard x-ray branch of the SOLEIL Metrology beamline

At the SOLEIL synchrotron (Saclay, France), the hard x-ray branch monochromator of the Metrology beamline is composed of a double Si(111) crystal whose Bragg angle is equipped with a rotary position encoder that requires an energy-angle calibration. The available energy range, defined by the extreme Bragg angles, is from 3 keV to 45 keV. An accurate calibration of the energy axis of the monochromator is obtained by using several pure metal foils as transmission targets and by performing energy scanning around their absorption edges. The first derivative of the recorded absorption curves is used to determine the accurate position of the absorption edge energies, which are then set to match the ones tabulated in Deslattes [8]. The residual difference between the angular position given by the encoder and the values derived from the tabulated absorption edges is presented in [9] and is kept below 0.04%. The minimization of harmonics or stray light are managed in the same way as detailed in [9]. The contributions of the harmonics are significant below 7 keV and in these cases, a small detuning of the second monochromator crystal is necessary to reduce their total contribution to 0.1%.

### 2.2 Characteristics of the CASTOR device

The CASTOR setup is a vacuum chamber equipped with a 7-axis manipulator. It is connected to the vacuum of the synchrotron beamline for each measurement campaign and must be removed afterwards, requiring a precise alignment prior to any experimental measurements. The most critical alignment is the coincidence between the vertical rotation axis and the beam path. Using a dedicated iterative procedure, the position of the CASTOR chamber perpendicular to the beam direction is defined by a motorized stage with an estimated precision of 20 to 30 micrometers.

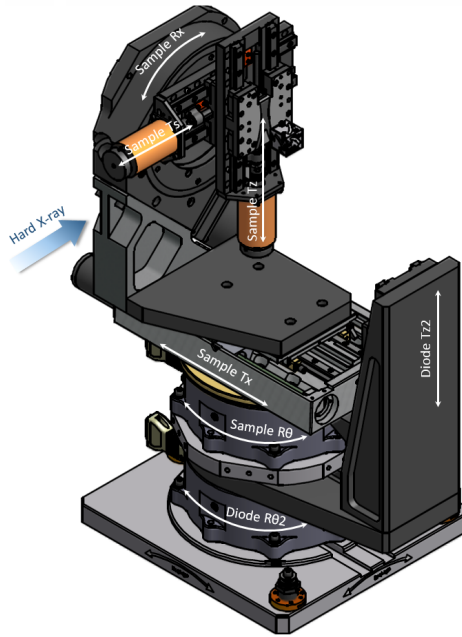


Figure 1: A schematic representation of the 7-axis goniometer. The beam [MAK] impinges the sample from the left, the surface of the sample being vertical.

The internal manipulator of CASTOR is composed of seven axes with five motors for the sample and two dedicated to the detection arm where several detectors are installed (see Figure 1). The samples are placed vertically on two perpendicular translation stages (namely Tz and Ts) which are mounted on a rotation stage (Rx). This three-axis platform is attached to a horizontal translation stage (Tx) which is on the upper rotation stage (Rθ). The detection arm is on a second rotation stage (Rθ2). The fourth translation (Tz2) allows selection of a detector. The Rθ and Rθ2 are the most critical axes for the experiments and are encoded for better accuracy. They can rotate freely except

that collisions are prevented by a limit switch on the  $R\theta$  arm. This configuration allows the sample manipulator and the detector arm to rotate freely within the chamber. The rotation stage Rx has a range of  $350^\circ$ . The translation stages have 110 mm ranges except for Tx which is limited to 102 mm.

The detection arm R $\theta$ 2 is equipped with four photodiodes and an energy-dispersive detector (e.g. Silicon Drift Detector (SDD)). The photodiode holders can be equipped with commutable slits or collimators. The current configuration is composed of four 100 mm<sup>2</sup> photodiodes from Opto Diode [10, 11] that have a typical efficiency of 0.27 A/W at 6 keV photon energy. In slot no. 1, an AXUV:Al photodiode is equipped with a 300  $\mu\text{m}$  vertical slit (used for alignment or measurements). The Al coating is necessary to prevent the infra-red or visible light degrading the dark current or background, improving the dynamic range of the reflectivity curves. Moreover, an AXUV100G photodiode without slit, placed in slot no. 2, was absolutely calibrated using a cryogenic electrical-substitution radiometer [12].

A spectrometer such as an energy-dispersive detector is required to perform fluorescence-related measurements such as GIXRF. It is installed on the chamber facing the sample (i.e. at  $90^\circ$  with respect to the incoming beam.). The experiments are performed with an SDD from AMPTEK (128 eV of energy resolution (FWHM) at 5.9 keV), which is mounted on a dedicated translation stage allowing it to approach as close as possible to the sample.

### 3 Combining x-ray reflectivity (XRR) and grazing-incidence x-ray fluorescence (GIXRF)

#### 3.1 Alignment and measurement procedure

The alignment of the CASTOR setup is crucial prior to any sample alignment. The main feature of it being the positioning of the pivot point in the path of the beam. For that purpose, we use a 300  $\mu\text{m}$  diameter pinhole placed on the sample holder to perform the scannings. The Tx translation stage (perpendicular to the beam when  $\theta = 0^\circ$  or  $180^\circ$ ) is scanned to find the centre position of the beam within the pinhole for  $\theta = 0^\circ$ . The same scan is performed for  $\theta = 180^\circ$  and the average between the two Tx positions provides the correct position for which the pivot is aligned with the beam. The whole chamber is moved according to this correction. We estimate the accuracy of the procedure to be in the range 10  $\mu\text{m}$ -20  $\mu\text{m}$  due to the precision of the translation stage of the chamber.

The second important point in aligning the experiment concerns the samples. For each sample, we use a well-known approach. We repeatedly scan on Tx and R $\theta$  until no change are found in the expected values with respect to the precision of the translation or rotation steps. With the translation stage Tx, we cut in half the incident beam intensity and by rotating the theta angle R $\theta$ , we set the sample at the maximum intensity. Nevertheless, in order to verify the accuracy, we add a scanning on the photodiode rotation stage R $\theta$ 2 at a fixed  $\theta$  angle (rocking curve) to account for a small theta offset.

At glancing angles (i.e. the very first points close to  $0^\circ$ ), geometrical effects disturb the x-ray reflectivity. At  $0^\circ$ , half of the incoming flux is directly measured by the photodiode. The limited length of the sample prevents the measurement of the real reflection intensity for angles lower than  $\sim 0.2^\circ$ . These geometrical effects are taken into account in our simulations.

#### 3.2 Example of XRR measurement and simulation

As a first example of our procedure, we recorded the reflectivity of a single layer sample at the photon energies of 6 keV and 11.4 keV. The layer is a mixture of nickel, cobalt and tungsten often used as electrode in the semiconductor industry. In order to compare the results at 6 keV and 11.4 keV, the incidence angle  $\theta$  is normalized to  $Q = 4\pi \times E \times \theta$  with photon energy  $E$  in keV. The Figure 3 left is presenting the comparison showing a very good agreement of the two reflectivities despite a small discrepancy at high angles due to a different noise level at the two incident energies. Moreover, the reflectivity at 6 keV was performed twice from  $0^\circ$  to  $10^\circ$  with steps of  $0.03^\circ$  and  $0.01^\circ$  in order to assess for the reproductibility when changing the steps. The measurements are presented in Figure 3 (right panel) as red and black curves respectively. The two measurements are perfectly reproducible until the reflectivity signal comes closer to the photodiode dark noise. These curves also show that the instrument is able to perform x-ray reflectivities with a dynamical range of six decades or more

despite the fact that the primary beam, delivered by a bending magnet, is unfocussed, its intensity being reduced by slits.

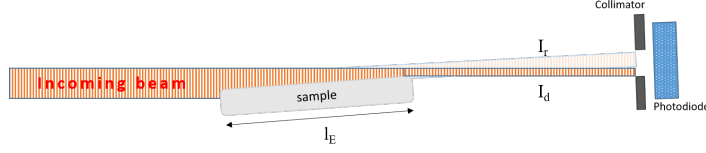


Figure 2: Geometry for the XRR at shallow angles.

In the case of the XRR, the theta scanning begins at  $0^\circ$ , for which the detected beam on the photodiode is the direct excitation beam cut in half. When increasing slowly the theta angle, the direct beam detection is progressively reduced ( $I_d$  on Fig. 2 left) and the reflected beam becomes dominant on the photodiode. The notch in the XRR close to  $0.08^\circ$ - $0.1^\circ$  correspond to the angle for which no further direct beam is detected on the photodiode. Its position and depth depend on the sample length ( $l_E$ ), photodiode distance, collimator width and incoming beam width. All these geometrical effects are taken into account in our model.

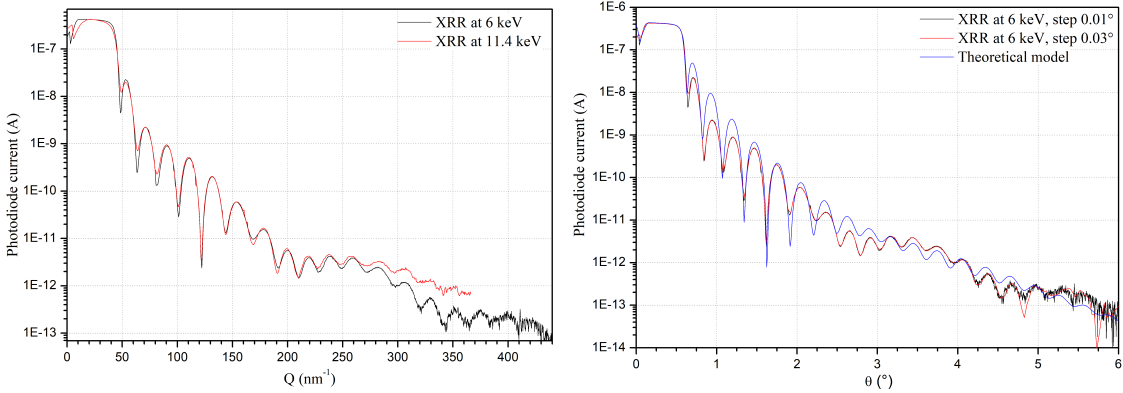


Figure 3: X-ray reflectivities of the single layer NiCoW sample. Left: comparison at 6 keV (black) and 11.4 keV (red). Right: comparison with steps of  $0.01^\circ$  (black) and  $0.03^\circ$  (red) at 6 keV, the model is in blue line.

To simulate the x-ray reflectivity of a sample, we use the Parratt recursive formula [1] together with the Nevot-Croce formalism [13] to account for the interface roughness. At glancing angles, the geometrical effects are limiting the reflectivity as the sample length is limited. The geometry is also taken into account for a better representative fitting at low scanning angle. Our fitting procedure uses a differential method as in [14] with a  $\chi^2$  cost function of  $XRR(\theta) \times \theta^5$ . The simulation (blue line) is performed with a three-layer model in order to account for density differences in the deposition process. The model results are presented in Table 1.

	Density ( $\text{g}\cdot\text{cm}^{-3}$ )	Thickness (nm)	Roughness (nm)
$NiCo_{0.11}W_{0.01}$	5.764	1.023	0.53
$NiCo_{0.11}W_{0.01}$	8.742	17.518	0.47
$NiCo_{0.11}W_{0.01}$	8.119	1.153	0.47
$SiO_2$	2.65	1.051	0.26
$Si$	2.3296		0.3

Table 1: Experimental model after the combined GIXRF-XRR analysis.

### 3.3 X-ray fluorescence detection solid angle

A dedicated acquisition software allows the CASTOR user to record the x-ray fluorescence emitted by the sample simultaneously or sequentially with the x-ray reflectivity, in order to combine both XRR and GIXRF. In both cases some geometrical aspects are of importance to model correctly the sample composition and structure in the fitting procedure. The footprint of the incoming beam on the sample is primarily defined by a slit. The samples being vertical, we use a vertical slit in order to limit the horizontal divergence of the beam and allow more flux by selecting larger height. We can use several slits of 100  $\mu\text{m}$  width and 1, 3 or 5 mm vertical aperture.

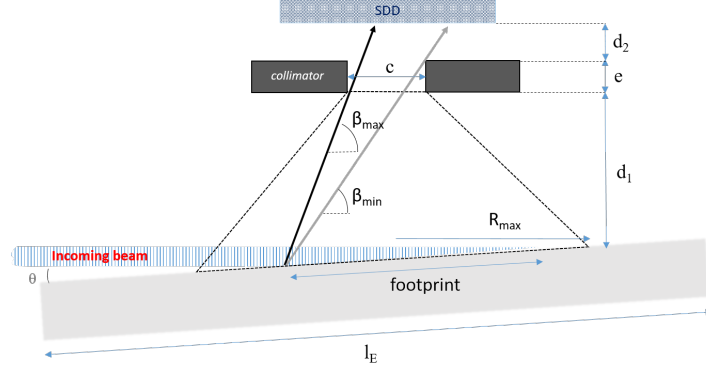


Figure 4: A schematic representation of the detection solid angle of the SDD. The measured distances are indicated as they are used for the estimation of the solid angle.

The x-ray fluorescence signal is acquired by the SDD for which the geometrical aspects are of major importance (fig. 4). A tungsten collimator (thickness  $e$  and diameter  $c$ ) is placed in front of the SDD and the distance to sample ( $d_1$ ) can be adapted manually. The solid angle is calculated accordingly to the measured distances and the dimensions of the collimator and the sample as well as the incoming beam characteristics (shape and dimensions). In a first step, we calculate the solid angle as a function of the radial distance  $r$  as every irradiated point on the sample will not contribute with the same importance to the signal of the SDD. The formula is given in Equation 1:

$$\Omega_r(r) = \iint_{S(r)} \frac{\text{Sin}(\beta)}{((d_1 + e + d_2)^2 + (r + x)^2 + y^2)} dx dy \quad (1)$$

where  $d_1$  is the distance between the sample and the collimator,  $e$  is the collimator thickness,  $d_2$  is the distance between the collimator and the SDD silicon chip. The angle  $\beta$  is given by  $\beta = \text{Arctan} \left( (d_1 + e + d_2) / \sqrt{(r + x)^2 + y^2} \right)$ . The integral limits are expressed as a surface  $S(r)$  which is the region common to several circles:  $S(r) = A_{SDD} \wedge A_{c1} \wedge A_{c2}$ , where  $A_{SDD}$  is the area of the SDD active area,  $A_{c1}$  and  $A_{c2}$  are the projected area on the SDD surface of the front and back side of the pinhole respectively.  $\Omega_r(r)$  takes positive values for  $0 \leq r \leq R_{max}$ ,  $R_{max}$  being the maximal off-axis distance.

In order to calculate the solid angle for every incident angle, the length of the sample ( $l_E$ ) and the spot size of the beam are required. The following formula (Equation 2) is applied at each individual incident angle:

$$\Omega(\theta) = \frac{1}{A_s} \iint_{A_s} \Omega_r(r) dx dy \quad (2)$$

where  $A_s$  is the area in common of the impinging beam spot, the size of the sample and the solid angle of the SDD delimited by the maximal radius  $R_{max}$ .

### 3.4 Simulation of the emitted x-ray fluorescence

To calculate the emitted fluorescence of a specific element from the sample, the evaluation starts with the calculation of the x-ray standing wave field inside the structure. The Parratt recursive algorithm

gives the value of forward and backward electric fields at the centre of each layer. In order to take into account the variation of the field and the interfaces roughnesses, our model cut the layers into thinner slabs. The detected fluorescence is derived using Equation 3:

$$XRF_i(\theta) = \frac{\Omega(\theta) I_0 T \eta_i \tau_i \omega_i \times \sum_j W_i(z_j) \rho(z_j) (z_j - z_{j-1}) \times \exp(-\sum_{h=1}^{j-1} \mu_i(z_h) \rho(z_h) (z_h - z_{h-1}))}{\|E_t(z_j, \theta) + E_r(z_j, \theta)\|^2} \quad (3)$$

where  $T$  is the acquisition live time of each spectrum,  $I_0$  is the flux of incident photons,  $\eta_i$  is the detector full energy peak efficiency at the line energy of element  $i$ ,  $\tau_i$  is the photoelectric cross sections of element  $i$  at incoming energy and  $\omega_i$  the partial fluorescence yields of element  $i$  (corresponding to the shell fluorescence yields combined with the line ratio). In case the line is feeded from several subshells due to the Coster-Kronig cascade, this has to be taken into account as well. The parameter  $W_i(z_j)$  corresponds to the weight fraction of element  $i$  at depth  $z_j$  and  $\rho(z_j)$  is the density at the same depth. The emitted fluorescence is reabsorbed when passing through the upper slabs and the exponential term in Equation 3 accounts for that. The solid angle  $\Omega(\theta)$  and the internal electric fields  $E_t(z_j, \theta)$  and  $E_r(z_j, \theta)$  must be calculated for each grazing angle. To meet our experimental setup, we derived the calculation of the x-ray standing wave field for  $P$  polarization. Thus, the electric field is replaced by  $H(z_j, \theta)/n$ .

As for the x-ray reflectivity, the fitting parameters are the layer densities, thicknesses, roughnesses and elemental weight ratio. The combination of both the XRR and GIXRF techniques that are using similar measurement procedures but different signals should provide better accuracy of these profiles.

### 3.5 Example of GIXRF

We performed a GIXRF experiment on the NiCoW sample. The photon exciting energy was chosen at 11.4 keV in order to get both the K lines of Ni and Co and the  $L_3$  lines of W. A typical spectrum is presented in Figure 5 showing the Co and Ni  $K\alpha$  and  $K\beta$  line contributions and the W  $L\alpha$  line. The overlapping lines are fitted with gaussians with standard deviations linked by a linear energy dependence to account for the spectrometer response, and they are perfectly distinguished by the spectrum processing software COLEGRAM [15].

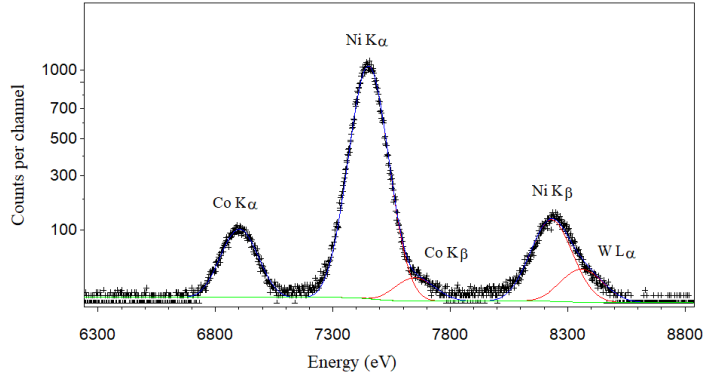


Figure 5: Experimental x-ray fluorescence spectrum at 11.4 keV and  $\theta = 0.44^\circ$ . The individuals peak functions appear in red, the complete fit in blue and the background in green.

We performed twice the experiment for two different distances of the SDD in order to validate the calculation of the solid angle. In order to have a good accuracy close to the maximum of the GIXRF curves in a reasonable experimental time, the software controlling the experiment allows the user to choose variable angular steps. We performed the GIXRF from  $0^\circ$  to  $2^\circ$ , with 60 or 30 seconds acquisition time per spectrum at  $d_1 = 15$  and 25 mm respectively. For all acquired spectra, we derived the peak areas of the useful lines with COLEGRAM in a batch processing mode. We simulate the XRR (Fig. 3) and GIXRF curves from our sample model and derived the best fitting parameters for the densities, thicknesses and roughness, which are presented in Table 1. The GIXRF curves are presented in Figure 6 and assess for an excellent agreement of the theoretical calculations with the experimental results.

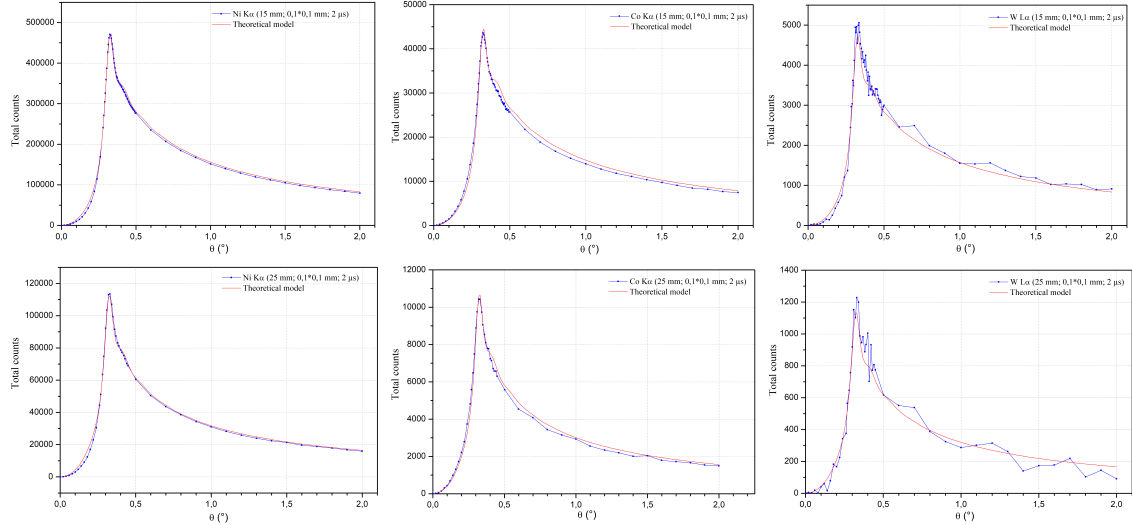


Figure 6: Experimental results of the fluorescence (peak area versus angle). From the left to the right, fluorescence of nickel, cobalt and tungsten. First line:  $d_1 = 15$  mm, second line:  $d_1 = 25$  mm. The red curves are the theoretical results from the model.

## 4 Example of application

As an application of our reference-free approach, we performed a combined XRR/GIXRF analysis on more complex samples. We used a three-layered sample and a periodic stack (three repetitions of two layers) of  $\text{Al}_2\text{O}_3/\text{HfO}_2$  in different combinations, deposited on Si with a native oxide layer. The layers were made by atomic layer deposition (ALD). The periodic stack is simulated by individualizing each layer, which leads to a potential large increase in the number of fitting parameters.

### 4.1 Three-layer sample

The incoming photons with an energy of 10 keV create vacancies in the K shell of aluminum, silicon and oxygen and in the  $L_3$  shell of hafnium, avoiding any Coster-Kronig transitions. The SDD is set at  $d_1 = 15$  mm and the incoming beam was cut at  $0.1 \times 0.5$  mm. We acquired 149 spectra of 150 s from  $0^\circ$  to  $3^\circ$ , of which we derived the hafnium  $L\alpha$  line area at every angular step. The spectra are processed using the COLEGRAM software [15] to get the individual peak areas, using Gaussian functions. The background of all spectra were processed to take into account the step due to the presence of a peak. As  $L\alpha_2$  could not be distinguished from  $L\alpha_1$ , the derived peak areas account for both line contributions. The experimental curves are presented in Figure 7. On the left, we compare the acquired XRR with the simulation and, in the centre, we compare the experimental Hf  $L\alpha$  line intensity with the result of the GIXRF calculation following our theoretical model. The excellent agreement between all experimental and theoretical curves gives confidence in the reliability of the parameters of the structure. In Figure 7 right, we give an overview of the depth-dependent densities derived by the model.

This sample was already studied in [16] by the same techniques but with different experimental equipment and excitation energies. The three-layered sample corresponds to the S2 sample of the article. In the published analysis, the  $\text{HfO}_2$  and  $\text{Al}_2\text{O}_3$  deposited materials were assumed to be stoichiometric and having bulk density,  $9.68 \text{ g.cm}^{-3}$  and  $3.987 \text{ g.cm}^{-3}$  for  $\text{HfO}_2$  and  $\text{Al}_2\text{O}_3$  respectively, which is not our case since significantly lower densities derived from our fit. In order to compare our results with the ones published in [16], we derive the areal mass for  $\text{HfO}_2$  and  $\text{Al}_2\text{O}_3$  from the layer densities and thicknesses and we present the results of [16] in Table 3 together with our results. Our results are in good agreement for  $\text{Al}_2\text{O}_3$  with PTB and CEA-LETI (Laboratoire d'électronique et des technologies de l'information), nevertheless a lower content maybe due to the difficulty to distinguish the aluminum  $K\alpha$  line from the large tail of the silicon  $K\alpha$  peak (photon energies lower than 3 keV are not accessible on the hard x-ray branch, it would be better to excite with an energy larger than Al K absorption edge and lower than Si K absorption edge to avoid the intense Si K peak in the spectra). Our result concerning  $\text{HfO}_2$  are in better agreement with LETI but significantly different from PTB.

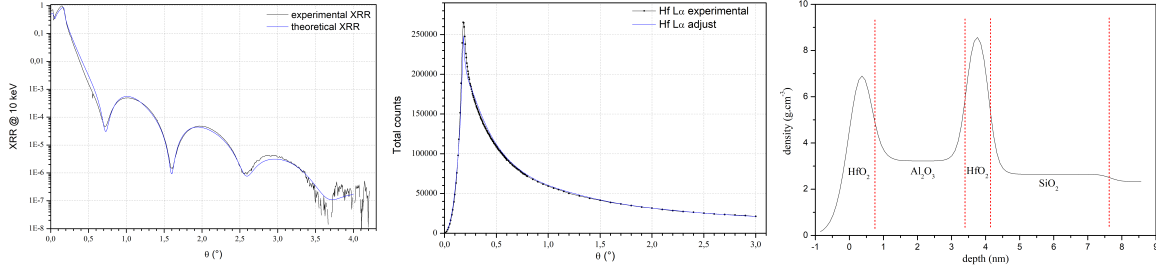


Figure 7: Three-layer sample: Experimental and theoretical XRR at 10 keV (left), GIXRF curve of Hf  $L\alpha$  line (centre), Fitted density from air to silicon substrate (right).

	Density ( $\text{g}\cdot\text{cm}^{-3}$ )	Thickness (nm)	Roughness (nm)
$HfO_2$	9.209	0.601	0.427
$Al_2O_3$	3.224	2.831	0.334
$HfO_2$	9.502	0.651	0.258
$SiO_2$	2.65	3.577	0.261
$Si$	2.3296		0.301

Table 2: Experimental model after the combined GIXRF-XRR analysis.

Unfortunately, our model cannot derive associated uncertainties as it is still a work in progress.

## 4.2 Periodic stack sample

The period of the stack is composed of two layers made of  $HfO_2$  and  $Al_2O_3$ , the complete stack being three repetitions of the period (see Table 4). The XRR was acquired at 6 keV and the GIXRF at 10 keV. Our model can handle combined analysis at different energies. The SDD is set at  $d_1 = 25$  mm and the incoming beam was cut at  $0.1 \times 3$  mm. We acquired 116 spectra of 60 s from  $0^\circ$  to  $7^\circ$  with a variable angular step in order to get more experimental points close to the critical angle. The spectra were adjusted the same way as previously to derive the peak area of the hafnium  $L\alpha$  line. The experimental XRR and GIXRF curves are respectively presented in Figure 8 left and middle; Figure 8 right presents the calculated depth-dependent densities.

As in the case of the three-layered sample, the periodic stack was studied in [16], assuming bulk densities. We scaled our thicknesses and found total thicknesses of 4.0 nm for  $Al_2O_3$  ( $4.7 \pm 0.7$  (PTB) and  $5.7 \pm 0.5$  (LETI) in [16]) and 5.0 nm for  $HfO_2$  ( $4.4 \pm 0.5$  (PTB) and  $5.1 \pm 0.3$  (LETI) in [16]). Once again, our excitation energy is not the best to derive the Al  $K\alpha$  intensities, this explains the rather weak agreement with other values. On the contrary, our deposited mass for  $HfO_2$  is in excellent agreement with the value derived by LETI.

## 5 Conclusion

We presented a combined XRR-GIXRF analysis of several samples. At first, we assessed our measurement procedure and calculation method on a well-known sample in different conditions in order to qualify our instrument and theoretical approach. Then, we applied our procedure to more complex samples in order to derive their interesting quantities. We found an excellent agreement between experimental results and fitted curves of both XRR and GIXRF which supports the confidence in the stack parameters derived.

	This work	PTB in [16]	LETI in [16]
$HfO_2$ ( $\text{ng}\cdot\text{mm}^{-2}$ )	11.7	6.8(10)	13.6(19)
$Al_2O_3$ ( $\text{ng}\cdot\text{mm}^{-2}$ )	9.13	10.4(16)	11.2(8)

Table 3: Comparison of the determined mass depositions by the different analyses.

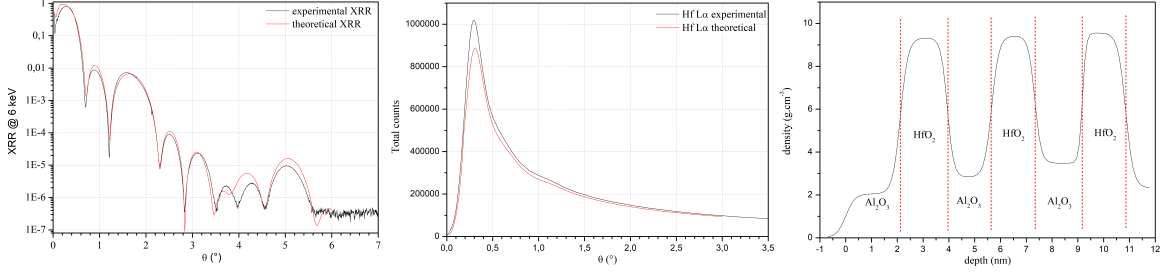


Figure 8: Periodic stack sample : Experimental and theoretical XRR at 6 keV (left), GIXRF curve of Hf  $L\alpha$  line (centre), Fitted density from air to silicon substrate (right).

	Density ( $\text{g}\cdot\text{cm}^{-3}$ )	Thickness (nm)	Roughness (nm)
$\text{Al}_2\text{O}_3$	2.052	2.118	0.353
$\text{HfO}_2$	9.332	1.818	0.300
$\text{Al}_2\text{O}_3$	2.824	1.72	0.246
$\text{HfO}_2$	9.425	1.671	0.285
$\text{Al}_2\text{O}_3$	3.482	1.849	0.247
$\text{HfO}_2$	9.559	1.676	0.140
$\text{Si}$	2.3296		0.300

Table 4: Experimental model after the combined GIXRF-XRR analysis.

## Acknowledgements

The authors are grateful to Pascal Mercere and Paulo Da Silva for assistance on the Metrology beamline and to the SOLEIL staff for smoothly running the facility and to Emmanuel Nolot for fruitful discussion and providing the samples. The authors are also grateful to Diane Eichert for the fruitful advices about the experimental alignment procedure.

## References

- [1] L. G. Parratt, “Surface Studies of Solids by Total Reflection of X-Rays,” *Physical Review*, vol. 95, no. 2, pp. 359–369, 1954.
- [2] D. K. G. de Boer, “Glancing-incidence x-ray fluorescence of layered materials,” *Physical Review B*, vol. 44, no. 2, pp. 498–511, 1991.
- [3] J. Lubeck, B. Beckhoff, R. Fliegauf, I. Holfelder, P. Hönicke, M. Müller, B. Pollakowski, F. Reinhardt, and J. Weser, “A novel instrument for quantitative nanoanalytics involving complementary X-ray methodologies,” *Review of Scientific Instruments*, vol. 84, p. 045106, 2013.
- [4] G. Das, S. R. Kane, K. Ajay, A. K. Singh, and M. K. Tiwari, “Simultaneous measurement of X-ray reflectivity and grazing incidence fluorescence at BL-16 beamline of Indus-2,” *Review of Scientific Instruments*, vol. 86, p. 055102, 2015.
- [5] D. Ingerle, M. Schiebl, C. Strelt, and P. Wobrauschek, “Combination of grazing incidence x-ray fluorescence with x-ray reflectivity in one table-top spectrometer for improved characterization of thin layer and implants on/in silicon wafers,” *Review of Scientific Instruments*, vol. 85, p. 083110, 2014.
- [6] M. Spanier, C. Herzog, D. Grötzsch, F. Kramer, I. Mantouvalou, J. Lubeck, J. Weser, C. Streeck, W. Malzer, B. Beckhoff, and B. Kanngiesser, “A flexible setup for angle-resolved X-ray fluorescence spectrometry with laboratory sources,” *Review of Sc*, vol. 87, p. 035108, 2016.
- [7] J. Lubeck, M. Bogovac, B. Boyer, B. Detlefs, D. Eichert, R. Fliegauf, D. Grötzsch, I. Holfelder, P. Hönicke, W. Jark, R. B. Kaiser, B. Kanngießer, A. G. Karydas, J. J. Leani, M. C. Lépy, L. Lühl,

- Y. Ménesguen, A. Migliori, M. Müller, B. Pollakowski, M. Spanier, H. Sghaier, G. Ulm, J. Weser, and B. Beckhoff, “A new generation of x-ray spectrometry UHV instruments at the SR facilities BESSY II, ELETTRA and SOLEIL,” *AIP Conference Proceedings*, vol. 1741, p. 030011, 2016.
- [8] R. D. Deslattes, E. G. Kessler, P. Indelicato, L. de Billy, E. Lindroth, and J. Anton, “X-ray transition energies: new approach to a comprehensive evaluation,” *Reviews of Modern Physics*, vol. 75, no. 1, pp. 35–99, 2003.
- [9] Y. Ménesguen, M. Gerlach, B. Pollakowski, R. Unterumsberger, M. Haschke, B. Beckhoff, and M.-C. Lépy, “High accuracy experimental determination of copper and zinc mass attenuation coefficients in the 100 eV to 30 keV photon energy range,” *Metrologia*, vol. 53, pp. 7–17, 2016.
- [10] Opto Diode Corporation (US). [Online]. Available: <http://optodiode.com/>
- [11] R. Korde, C. Prince, D. Cunningham, R. E. Vest, and E. Gullikson, “Present status of radiometric quality silicon photodiodes,” *Metrologia*, vol. 40, pp. S145–S149, 2003.
- [12] P. Troussel and N. Coron, “BOLUX: a cryogenic electrical-substitution radiometer as high accuracy detector in the 150-11000 eV range,” *Nuclear Instruments & Methods in Physics Research, Section A: Accelerators, Spectrometers, Detectors, and Associated Equipment*, vol. 614, pp. 260–270, 2010.
- [13] L. Nénot and P. Croce, “Caractérisation des surfaces par réflexion rasante de rayons X. Application à l’étude du polissage de quelques verres silicates,” *Revue de Physique Appliquée*, vol. 15, pp. 761–779, mars 1980.
- [14] G. Ingerle, D. and Pepponi, F. Meirer, P. Wobrauschek, and C. Streli, “JGIXA - A software package for the calculation and fitting of grazing incidence X-ray fluorescence and X-ray reflectivity data for the characterization of nanometer-layers and ultra-shallow-implants,” *Spectrochimica Acta, Part B: Atomic Spectroscopy*, vol. 118, pp. 20–28, 2016.
- [15] Y. Ménesguen and M.-C. Lépy, “COLEGRAM, a flexible user-friendly software for processing of ionizing radiation spectra,” *Nuclear Instruments and Methods in Physics Research Section A: Accelerators, Spectrometers, Detectors and Associated Equipment*, vol. 1003, p. 165341, 2021. [Online]. Available: <https://www.sciencedirect.com/science/article/pii/S0168900221003259>
- [16] P. Hönicke, B. Detlefs, M. Müller, E. Darlatt, E. Nolot, H. Grampeix, and B. Beckhoff, “Reference-free, depth-dependent characterization of nanolayers and gradient systems with advanced grazing incidence X-ray fluorescence analysis,” *Physica Status Solidi A*, vol. 212, no. 3, pp. 523–528, 2015.